

Article

The Chemical Characteristics and Metallogenic Mechanism of Beryl from Cuonadong Sn-W-Be Rare Polymetallic Deposit in Southern Tibet, China

Yiyun Wang *, Guangming Li, Wei Liang and Zhi Zhang

Chengdu Center, China Geological Survey, Chengdu 610081, China; li-guangming@163.com (G.L.); lwcugb@126.com (W.L.); tancer_1314@126.com (Z.Z.)

* Correspondence: wangyiyun1988@163.com

Abstract: The Cuonadong deposit is the first large scale Sn-W-Be rare polymetallic deposit located in southern Tibet, China, where beryl is the main beryllium-bearing mineral. In this paper, the beryl crystals in the pegmatitic and hydrothermal vein orebody from the Xianglin area of the Cuonadong deposit are the research objects, marked as Beryl-I and Beryl-II, and they are investigated by EPMA, LA-ICP-MS and in situ micro-X-ray diffraction (XRD). Data by EPMA and LA-ICP-MS reveal that beryls from this area are alkaline beryls, among which Beryl-I is composed of Li-Cs beryl, and Beryl-II is composed of Na beryl and Na-Li beryl, indicating that beryls have undergone noticeable alkali metasomatism during formation. The Cs/Na ratio in Beryl-I ranges from 0.10 to 0.44, and the Mg/Fe ratio is almost 0, showing that Beryl-I is formed under high-differentiation evolution conditions and is rarely affected by hydrothermal transformation, whereas the Mg/Fe ratio in Beryl-II ranges from 2.73 to 17.31, and the Cs/Na ratio is nearly 0, indicating that Beryl-II has been obviously affected by late hydrothermal metasomatism. In situ XRD analysis shows that both Beryl-I and Beryl-II are *t*-beryl, and the *c/a* ratio of Beryl-I (1.0010–1.0012) is slightly higher than that of Beryl-II (1.0005–1.0008), which may also reflect the transition from magmatism to hydrothermal metasomatism in the late stage of pegmatitic magmatism. Based on comprehensive analysis, we believe that the precipitation of Beryl-I is mainly caused by the emplacement of highly fractionated magma containing Be to the top of the rock mass or surrounding rock, the melt-fluid undercooling, and the crystallization of volatile-bearing minerals (such as tourmaline and fluorite). Moreover, the Be-bearing ore-forming fluid has further migrated upward along the near north–south faults formed in the middle Miocene (16–15 Ma), during which Beryl-II precipitates owing to the hydrothermal water mixing, the ore-forming fluid cooling, and large amounts of crystallization of volatile-bearing minerals (mainly fluorite). Therefore, it can be concluded that beryl mineralization largely reflects the process of magmatic–hydrothermal mineralization. Because of a large number of mineralized areas with the similar metallogenic backgrounds to the Cuonadong deposit in the Himalayan region, it has great potential to be a new globally significant rare metal metallogenic belt.



Citation: Wang, Y.; Li, G.; Liang, W.; Zhang, Z. The Chemical Characteristics and Metallogenic Mechanism of Beryl from Cuonadong Sn-W-Be Rare Polymetallic Deposit in Southern Tibet, China. *Minerals* **2022**, *12*, 497. <https://doi.org/10.3390/min12050497>

Academic Editor: Aleksei V. Travin

Received: 21 February 2022

Accepted: 15 April 2022

Published: 19 April 2022

Publisher's Note: MDPI stays neutral with regard to jurisdictional claims in published maps and institutional affiliations.

Keywords: beryl; rare metal; element substitution; metallogenic mechanism; Cuonadong; Himalayan metallogenic belt



Copyright: © 2022 by the authors. Licensee MDPI, Basel, Switzerland. This article is an open access article distributed under the terms and conditions of the Creative Commons Attribution (CC BY) license (<https://creativecommons.org/licenses/by/4.0/>).

1. Introduction

Beryllium, the lightest alkaline earth metal element, is highly incompatible; thus, it is commonly present in granitic residual melts and enriched in evolved granites and granitic pegmatites [1,2]. The formation of beryllium minerals runs through the whole magmatic–hydrothermal evolution process, including beryl, chrysoberyl, phenacite and bertrandite [3–6]. Beryl is the most common beryllium mineral, which is mostly present in peraluminous metallogenic systems and can be formed at multiple stages of the magmatic–hydrothermal transition. According to the evolution stage of the magma–hydrothermal

system, it is further divided into three types: magmatic, granitic pegmatite and hydrothermal type [1,7]. Beryl is the most important Be-hosting mineral in granitic pegmatite-type beryllium deposits [6]. During the magmatic–hydrothermal evolution of granitic pegmatite, the crystallization of beryl is predominantly controlled by temperature and pressure [6]. In addition, the stability of beryl in the melt is also affected by the activity of Si, Al and other components in the melt, such as Li, B, P, F, Rb, Cs, etc. [4,5]. Small changes in activity of Be^{2+} can alter the crystallization behavior of beryl with changes in the composition and temperature of the pegmatitic melt [2,5].

In addition to being an important carrier of Be, beryl can also carry a certain amount of Li, Cs, Na, Fe, Mg, and its chemical composition and structure can be used to indicate the degree of differentiation of pegmatites and trace magmatic–hydrothermal evolution [8,9]. Studies have shown that the higher the Cs content in beryl is, the lower the Na/Cs value, Na/Li value, Mg/Fe value and Mg content are, indicating the higher degree of differentiation and evolution of granitic pegmatite [8–11].

Beryl, ideally $\text{Be}_3\text{Al}_2\text{Si}_6\text{O}_{18}$, has a ring structure consisting of layers of rings with six Si-O tetrahedra (T1), which are linked vertically and laterally by Be-O tetrahedra (T2) and Al-O octahedra (O), and the centers of the Si rings contain channels [12,13]. Various cations may be incorporated in the beryl structure, resulting in complex substitutions [6]. Therefore, the crystal structure and chemical composition of beryl can reflect the physical and chemical conditions of its formation [1,2,9–13].

The Cuonadong W-Sn-Be rare polymetallic deposit, located in southern Tibet, China, was first discovered in the Himalaya region in recent years, with superlarge-scale prospecting potential [14,15]. The mineralization types are complex, including the pegmatite Be orebody in Miocene pegmatitic leucogranite, the skarn W-Sn-Be orebody in the strongly deformed mantle of the dome, and the hydrothermal vein-type Sn-W-Be orebody faulted by north–south-trending rifts (NSTRs). Preliminary exploration of the W-Sn-Be orebody in the skarn around the dome mantle of the resources are $\text{WO}_3 > 50,000$ tons (average grade 0.21%), Sn $> 80,000$ tons (average grade 0.36%), and BeO $> 170,000$ tons (average grade 0.09%) [14,15], and they have attracted the attention of many scholars, mainly focusing on geological characteristics [16,17], petrology [18–21], chronology [22–29], geochemistry [30,31] and basic mineralogy [32–34]. Beryl is the most important beryllium-bearing mineral in the Cuonadong deposit [17,28]. Although some scholars have conducted some preliminary research on the composition of beryl in this deposit, they have conducted a rough discussion on the element substitution mechanism of beryl and its effect on pegmatites [33,34]. However, the research on the formation mechanism of beryl is incomplete.

In this study, beryl crystals from pegmatitic and hydrothermal mineralization in the Cuonadong deposit as the research objects are investigated by energy spectrum scanning, electron probe, LA-ICP-MS, in situ microzone XRD, with a view to ascertain the physical and chemical characteristics of beryl from the two types of mineralization, and to discuss the Cuonadong deposit in the magmatic–hydrothermal evolution process of the rare metal Be metallogenic mechanism, which can provide evidence of the Himalayan metallogenic belt having further prospects in rare metals.

2. Geologic Setting

2.1. Himalayan Metallogenic Belt

The Tethyan Himalaya Sequence (THS) is separated by the Indus Yarlung Tsangpo suture zone to the north and the South Tibet Detachment System (STDS) to the south [35–37], sandwiched between the Great Himalayan Crystalline Complex (GHC) and the Lhasa terrane [38] (Figure 1). As the largest highly differentiated granite belt developed in the Himalayas, the study of Cenozoic tectono-magmatic evolution and metallogenic relationship between highly differentiated leucogranites and their rare metals in this region has been a hot topic at home and abroad in recent years.

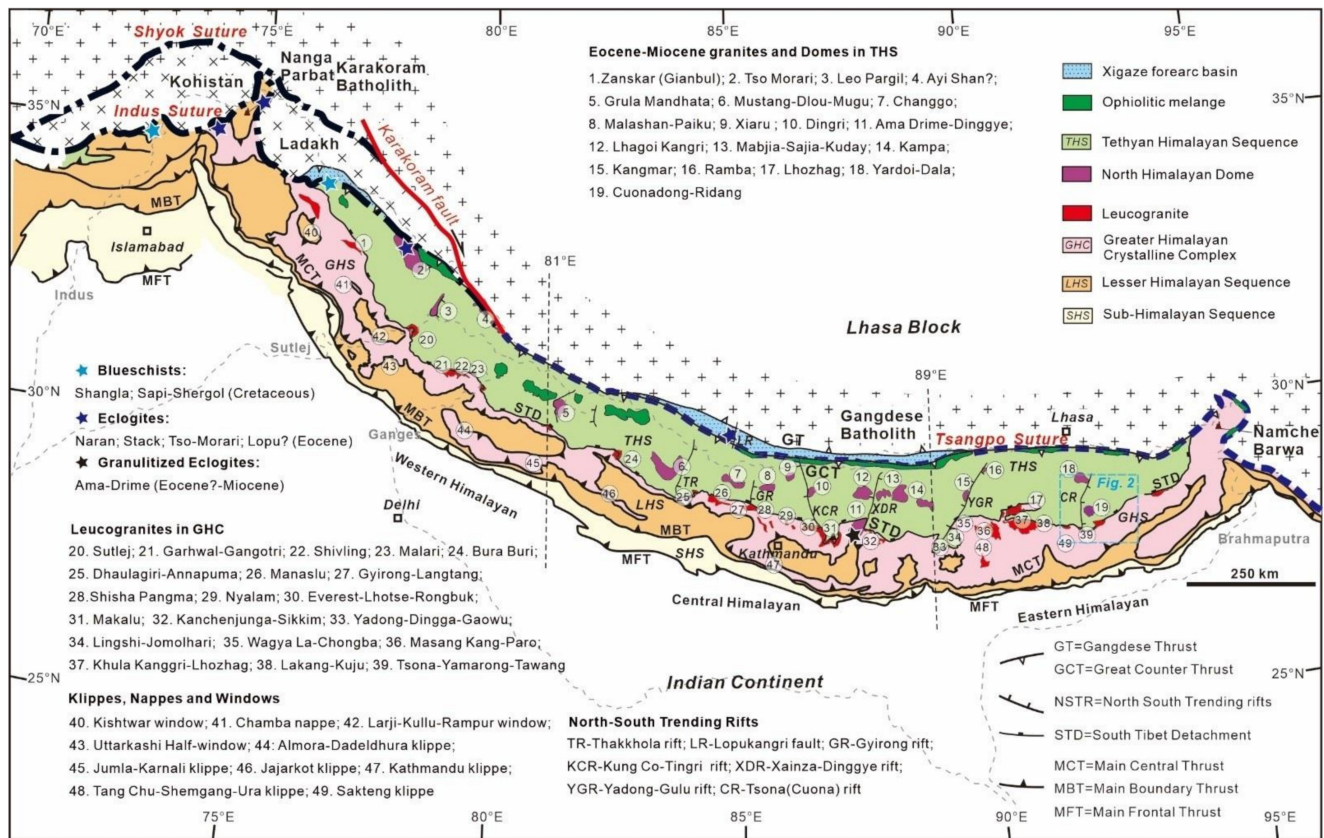


Figure 1. Map of the Himalayan orogenic belt showing the distribution of leucogranites, gneiss domes, tectonic zones and the Cuonadong deposit [27].

Previous studies revealed that the Himalayan Metallogenic Belt is mainly composed of Pb-Zn-Ag-Au-Sb deposits [39–43]. Meanwhile, researchers have been paying attention to the mineralization of rare metals such as beryllium, tungsten, and tin in the Himalayas. Many rare metal minerals have been found in leucogranites and pegmatites, including lithium-rich minerals such as lithium tourmaline and spodumene [44], and other rare metal minerals such as scheelite, cassiterite, beryl, niobium rutile, columbite–tantalite, iron-lepidolite, spodumene, rubidium-containing mica, etc. [44–48]. Beryl, as a beryllium-rich mineral, was found in the Pusila, Wengbo, Cuona, Yadong, Kangma, Gaowu, Dingjie, Xiaru, Peguco and other leucogranite bodies [47]. The latest exploration results show that Be-Rb-Nb-Ta-W-Sn and other rare metal mineralizations are developed in and around the Himalayan domes (Figure 1). Preliminary studies show that this region has great metallogenic potential and is expected to become an important rare metal metallogenic belt in China [47–50].

2.2. Geology of Cuonadong Mining Area

The spatial distribution of the Cuonadong Sn-W-Be polymetallic deposit is strictly controlled by the structure of the Cuonadong gneiss dome, which is typically representative of rare metal mineralization in the Himalayan gneiss dome belt [14–17].

2.2.1. Cuonadong Gneiss Dome

The Cuonadong gneiss dome is shaped as a rhombus, which is 20 km in length, 20 km in width and approximately 400 km² in area. The dome can be divided into three parts: core, mantle and rim [15,19,22] (Figure 2). First, the core is located under the lower detachment fault, consisting of early Paleozoic orthogneiss and Miocene leucogranite and pegmatite. Furthermore, the mantle and core are separated by the lower ductile detachment fault. The mantle shows typical characteristics of the ductile shear zone, formed from a set of

strongly deformed quartz–mica schists with mylonitized carbonate rocks metamorphosed at Paleogene. Strong contact metasomatism occurred between the marble and leucogranite or granitic pegmatite, thus forming a discontinuous skarn zone around the dome where W–Sn–Be polymetallic ore bodies are found. In addition, the rim and mantle are separated by the upper brittle detachment fault, and the rim is dominated by a set of low-grade metamorphic rocks composed of phyllite, sandy slate and carbonaceous slate.

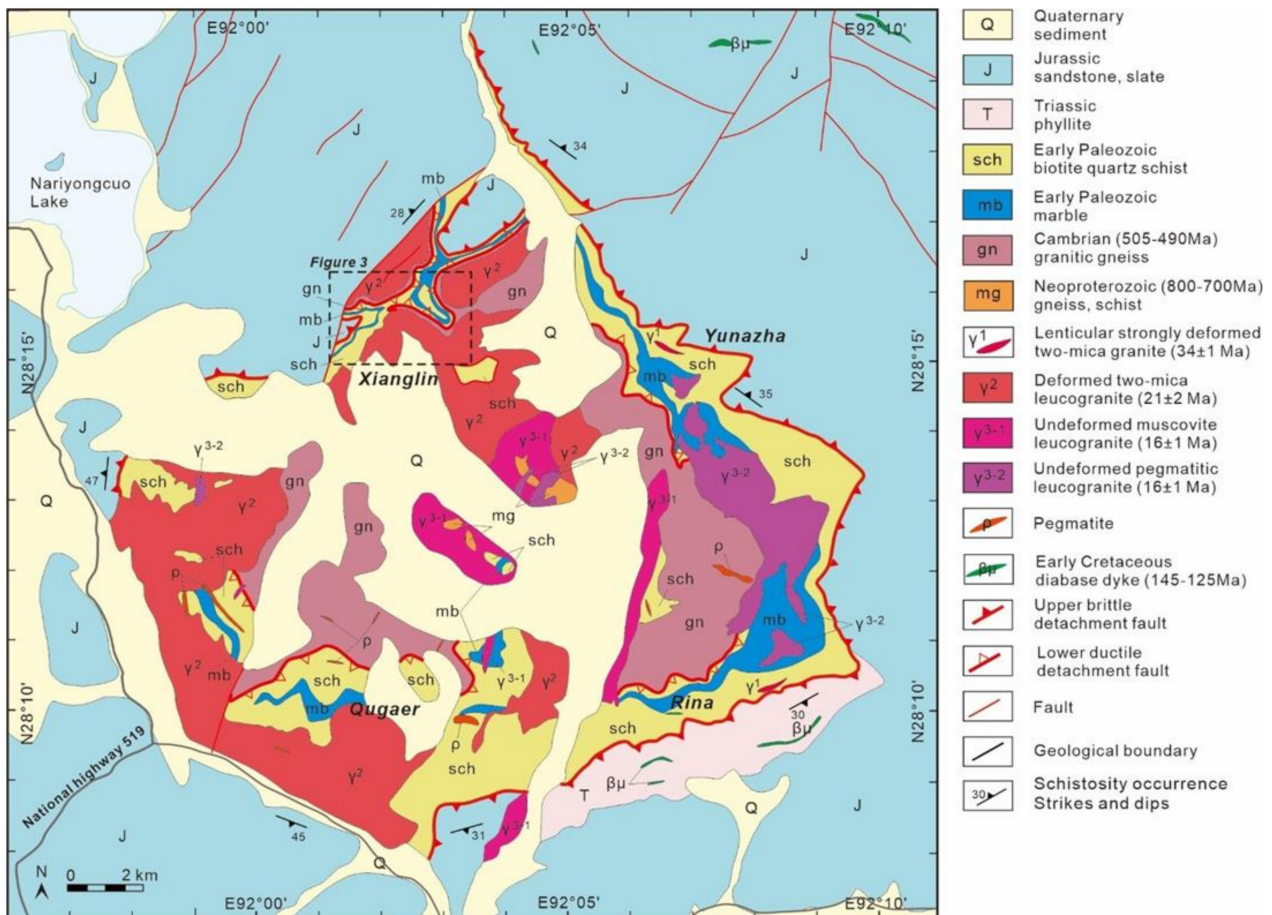


Figure 2. Geological map of the Cuonadong dome [16].

The Cuonadong dome has experienced three strong magmatism stages. The first stage occurred under the background of the dome activity of the south Tibet detachment system (STDS) in southern Tibet in the Oligocene (34~26 Ma) and was mainly distributed in the mantle and rim of the dome [50]. The lithology is mainly composed of strong deformed two-mica granites and granitic pegmatite. The second stage occurred in the lower detachment fault in the Early Miocene (24~18 Ma) [8,10]. The lithology consists of two-mica granites with weak deformation. Particularly in the vicinity of the lower detachment fault, the second-phase two-mica granite is directed with schist and marble and shows strong mineral orientations and lenticular shapes [18,20,30]. ③ The third stage occurred in the Middle and Late Miocene (16~14 Ma) with undeformed massive muscovite leucogranite and highly differentiated garnet–tourmaline-bearing muscovite leucogranite and beryl-bearing pegmatite [27,31]. The main body of the dikes is mainly distributed in a north–south direction, intrudes into various geological bodies and structural layers, and cuts the detachment fault in the form of veinlets, which is probably related to the north–south-trending rifts (NSTRs) (Figure 2).

2.2.2. Mineralization Characteristics

Four regions with important metallogenic potential are distributed around the dome, including Xianglin, Yunazha, Rina and Qugaer (Figure 2). Among them, the Xianglin area in the northwestern part of Cuonadong has the most abundant mineralization types and the largest inferred resources; thus, it is the key research area in this study and the main area of recent mineral exploration (Figure 3).

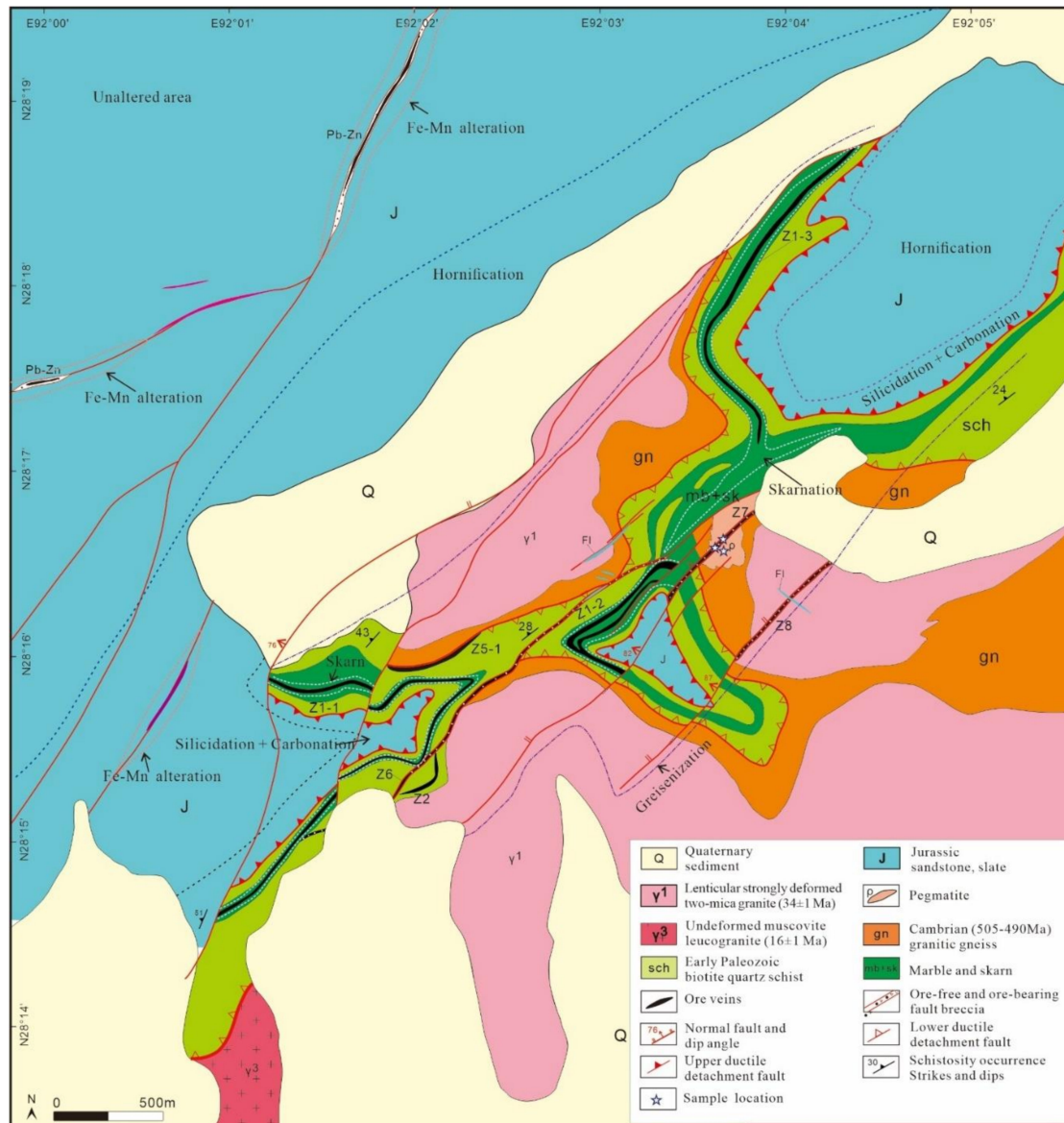


Figure 3. Geological map and sample location of Xianglin in the Cuonadong deposit.

The main mineralization types at Xianglin include pegmatite Be, skarn W-Sn-Be and hydrothermal vein Sn-W-Be ores. Preliminary exploration of Xianglin shows that the resources of Sn, WO_3 and BeO are over 80,000 t at 0.36%, 50,000 t at 0.21% and 34,000 t at 0.08% [27,28].

- ① The pegmatite Be orebody is spatially closed to muscovite granite (16 ± 1 Ma), and a large amount of beryl-bearing pegmatite is developed on the top of the muscovite granite. The gradual and transitional contact between the two implies an evolutionary relationship. Beryl is the main beryllium-bearing mineral in the disseminated form, with crystals up to 10 cm and colors ranging from blue–green to pale green, which

co-exists with quartz, plagioclase, K-feldspar, muscovite, tourmaline and fluorite (Figure 4a). The content of beryl in pegmatite dikes is not evenly distributed, and the scale of individual veins is tens of centimeters to a few meters, which has not yet been evaluated [14,17].

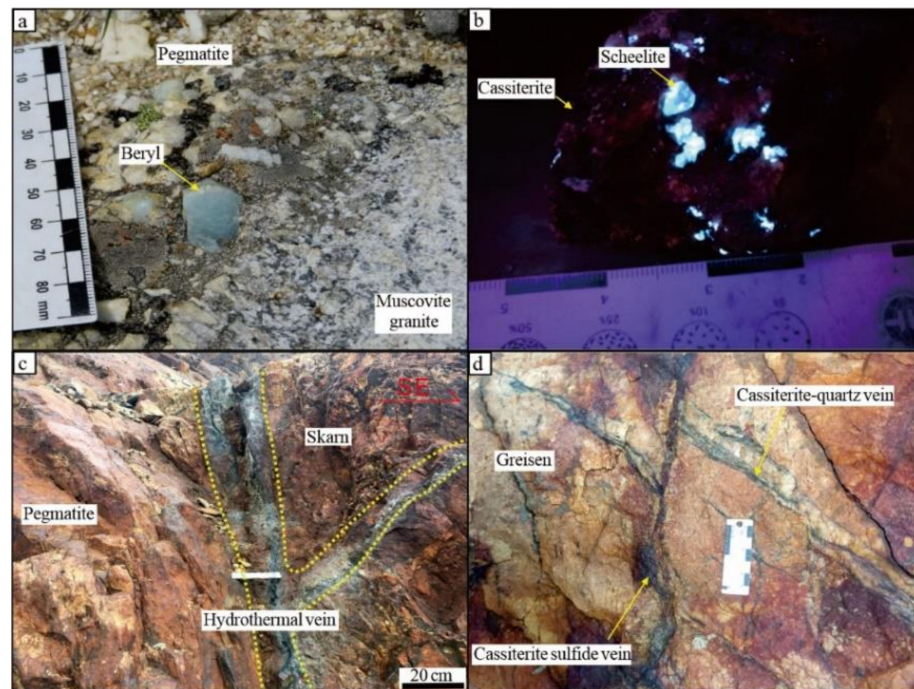


Figure 4. Typical mineralization at Cuonadong deposit. (a): The contact zone between muscovite granite and pegmatite, in which a beryl crystal has a hexagonal section. (b): Skarn-type ores under ultraviolet light showing scheelite (distinct light blue color). (c): Ore-bearing hydrothermal veins interspersed in viritic rock and skarn. (d): In the greisen, the cassiterite-quartz vein was cut by the cassiterite sulfide vein.

- ② Skarn ore bodies are mainly W-Sn mineralization, followed by Be. Cassiterite is the dominant tin-bearing mineral, and scheelite is the main tungsten-bearing mineral (Figure 4b). Beryllium mainly occurs in silicate minerals, such as vesuvianite, albite and garnet, through element substitutions and a small amount of Be-containing minerals such as phenacite, bertrandite [32]. However, as far as the current mineral processing technology is concerned, beryllium in these skarn minerals is difficult to fully utilize [51].
- ③ Hydrothermal vein ore bodies are produced in high-angle and nearly north-south faults and detached faults, mainly exhibiting greisenization, albitization, silicification, fluoridization and pyritization. The mineralization includes cassiterite-quartz veins (Figure 4c) and cassiterite sulfide veins (Figure 4d), which is superimposed on skarns, or occurs on the top or in the edge of granitic pegmatites, which developed later than weakly oriented mica granites, indicating that hydrothermal veins may be formed in garnet-bearing mica granites. The latest exploration results show that 11 new hydrothermal vein Sn-W-Be ore bodies have been discovered in the Xianglin area, among which one main ore body (No. Z6 orebody) has the predicted potential resources of Sn 73,800 tons at 1.75%, WO_3 19,900 tons at 0.36% and BeO 3100 tons at 0.14% [51]. Beryllium occurs mainly in beryl, and tin and tungsten occur in cassiterite and scheelite, respectively. The hydrothermal vein Sn-W-Be ore bodies are the most significant mineralization in the Cuonadong mining area [17,51].

3. Analytical Methods

In this paper, two beryl crystals from pegmatitic and four from hydrothermal mineralization of the Xianglin area are taken as the key research objects (Figure 5), and the location of the samples is shown in Figure 3.

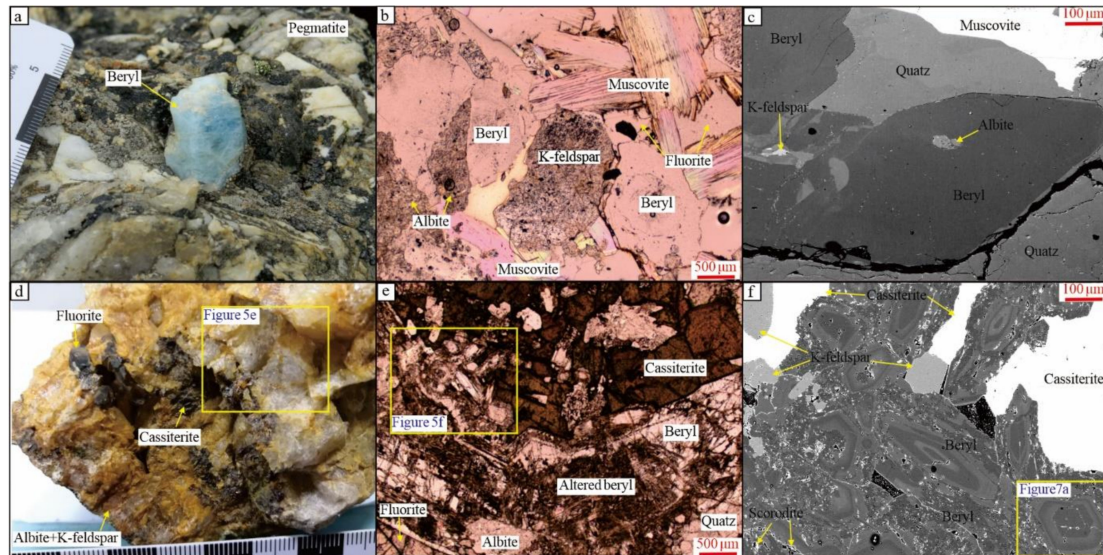


Figure 5. Occurrence characteristics of beryl in the Xianglin area. (a): Beryl-bearing pegmatite. (b): beryl co-existing with quartz, plagioclase, K-feldspar, muscovite and fluorite (plane-polarized light). (c): beryl co-existing with quartz, plagioclase, K-feldspar, muscovite (BSE image); (d) Beryl- and cassiterite-bearing hydrothermal vein. (e) Beryl with band structure, associated with cassiterite, quartz, muscovite and albite (plane-polarized light). (f): Beryl with complex zonal structures, associated with cassiterite, K-feldspar, quartz, muscovite, albite and scorodite (BSE image).

The samples under investigation were characterized through a combination of optical examination, combined with scanning electron microscopy, electron microprobe analyses and laser ablation inductively coupled plasma mass spectrometry.

Major- and minor-element compositions of beryls were conducted on a JEOL JXA-8230 electron microprobe at the Key Laboratory of Metallogeny and Mineral Resource Assessment, Institute of Mineral Resources, Chinese Academy of Geological Sciences. The analytical conditions were: an accelerating voltage of 15 Kv, a beam current of 20 nA, and a beam size of 5 μm . The following standards were used: albite (Na), sanidine (Si,Al,K), pyrope (Mg), titanite (Ca,Ti), almandine (Fe), rhodonite (Mn), Rb-leucite (Rb) and pollucite (Cs). The analytical data were corrected using the ZAF methods.

Trace-element compositions of beryls were performed using an X-Series ICP-MS (Thermo Fisher Scientific, Braunschweig, Germany) coupled with a J-200 343 nm Yb: Fiber femto-second laser ablation system (Applied Spectra, West Sacramento, CA, USA) housed at the National Research Center for Geoanalysis, Chinese Academy of Geological Sciences. Helium gas carrying the ablated sample aerosol from the chamber was mixed with argon make-up gas and nitrogen as an additional diatomic gas to enhance sensitivity. A baffled-type smoothing device was used in front of the ICP-MS to reduce fluctuation effects induced by laser-ablation pulses and to improve the quality of the data [52]. The beryl samples were ablated for 50 s at a repetition rate of 8 Hz at 6 J/cm², and ablation pits were ~50 μm in diameter. The calibration was performed externally using two NIST SRM 610 and one NIST SRM 612 for every 10 samples with ²⁹Si, measured by electron microprobe, as the internal standards to correct for instrument drift. Data reduction was carried out with the commercial software ICPMS Data Cal 10.8 [53,54]. The detection limits of LA-ICP-MS ranged from 0.05 to 0.1 ppm for REE. Repeated analyses of the standards

SRM 610 and SRM 612 indicate that both precision and accuracy were better than 10% for most analyzed elements.

The mapping of beryl was determined using a NWR 193 nm ArF Excimer laser-ablation system coupled to an iCAP RQ (ICPMS) at the Guangzhou Tuoyan Analytical Technology Co., Ltd., Guangzhou, China. The ICPMS was tuned using NIST 610 standard glass to yield low oxide production rates. Then, 0.7 L/min He carrier gas was fed into the cup, and the aerosol was subsequently mixed with 0.89 l/min Ar make-up gas. The laser fluence was 5 J/cm², with a repetition rate of 20 or 30 Hz and a 5, 8 or 10 μm spot size. The laser scan speed was 15, 20 or 35 μm/s. The raw isotope data were reduced using the “TRACE ELEMENTS” data reduction scheme (DRS). The DRS runs within the freeware IOLITE package of Paton [55]. In IOLITE, user-defined time intervals are established for the baseline correction procedure to calculate session-wide baseline-corrected values for each isotope. Blocks of two standards (one NIST 610 and one GSE-2G) and one MASS-1 sulfide standard analyses were followed by 5 to 8 unknown samples. ²⁹Si in beryl measured by electron microprobe was used as internal standard to correct instrument drift.

In situ micro-X-ray diffraction (XRD) experiment was conducted with a Rigaku D/max Raxis IIR micro-XRD system at the Guangzhou Institute of Geochemistry, Chinese Academy of Sciences. All measurements were carried out at the 40 kV and 250 mA (Cu Kα radiation) with a collection time of 22 min, 2θ range is 20–110 °C, and continuous scan. The scan speed was 4°/min. The X-ray beam was about 40 μm in diameter, focused on the selected spots on the thin sections. The data point interval was 0.045°. The software of MDI Jade 6.0 (International Centre for Diffraction Data, Denver, CO, America) was used to analyze the obtained XRD patterns for the derivation of unit-cell parameters by whole pattern fitting.

4. Results

4.1. Occurrence

Beryl from pegmatite (Beryl-I) is mostly symbiotic with rock-forming minerals such as quartz, potash feldspar, albite, muscovite and fluorite, with well-developed hexagonal column shape and particle sizes of 0.1–5 cm (Figure 5a,b). BSE images of these beryl particles show a homogeneous structure and locally developed altered edges, which is metasomatized by quartz, muscovite, K-feldspar, and albite along the edges or fissures (Figure 5b,c).

Beryl from the hydrothermal veins (Beryl-II) is mainly associated with cassiterite, scheelite, quartz, muscovite, phlogopite, fluorite, albite, sphalerite, and arsenopyrite, with the sizes ranging from 0.1 to 20 mm (Figure 5d,e). It is typically characterized by the development of complex zonal structures, which are locally replaced or dissolved by later K-feldspar, albite, and scorodite (Figure 5e,f).

4.2. Chemical Composition

As Li and Be are light elements (i.e., the X-ray yield through electron excitation is poor), and it is not possible to obtain precise Li₂O and BeO analyses on an electron microprobe. Furthermore, Be is a major element in beryl; thus, the results measured by LA-ICP-MS are inaccurate [33]. Assuming that the crystallochemical formula of beryl is X₃Y₂[Z₆O₁₈], the anion method is adopted for calculation, and the theoretical number of oxygen atoms is 18 [56]. The theoretical atomic number of Be, herein, is calculated by taking the sum of the cations at the X site as 3. Meanwhile, assuming that Be at the X site is only replaced by Li, the theoretical atomic number of Be can be calculated by Be = 3-Li *apfu* [56]. The quantification of H₂O was estimated as H₂O wt.% = (0.845958 × Na₂O in wt.%) + 0.08373 [57].

In this paper, two methods are used to obtain the Li content in beryl, one is through chemical calculation of EPMA (Li = Ca + Na + K + Cs, the number of atoms obtained by stoichiometric calculation) [58], the other is direct determination by LA-ICP-MS. By comparing the data results of these two methods, we found that Li content in beryl calculated by EPMA (0.04–0.87 wt.%) is significantly higher than that directly determined by LA-ICP-MS (1.23–2.48 wt.%). The reason is that there is complex metal replacement in

beryl [59]. Li^+ replacement of Be^{2+} results in a charge deficit, which requires monovalent alkali metal to enter the channel to balance the charge. This is the same as the replacement process of Al^{2+} by Fe^{2+} and Mg^{2+} [34].

Beryls from the Xianglin area contain different amounts of FeO (0.17–1.31 wt.%) and MgO (0–2.06 wt.%), leading to the high content of Li obtained by chemical calculation of EPMA. It implies that the content of Li in beryls is not completely consistent with the sum of other alkali metals (Figure 6). Thus, the content of Li calculated by using the EPMA component may lead to deviation. Moreover, the deviation of the Li content calculation value will further affect the content of BeO. Therefore, in this paper, the content of Li directly measured by LA-ICP-MS is used to calculate the content of BeO. By calculation, the BeO content of beryl in pegmatite is 11.69–12.05 wt.%, and that in the hydrothermal vein is 12.27–13.75 wt.%. The H_2O content of the two beryls is 1.41–1.60 and 1.26–2.25 wt.%.

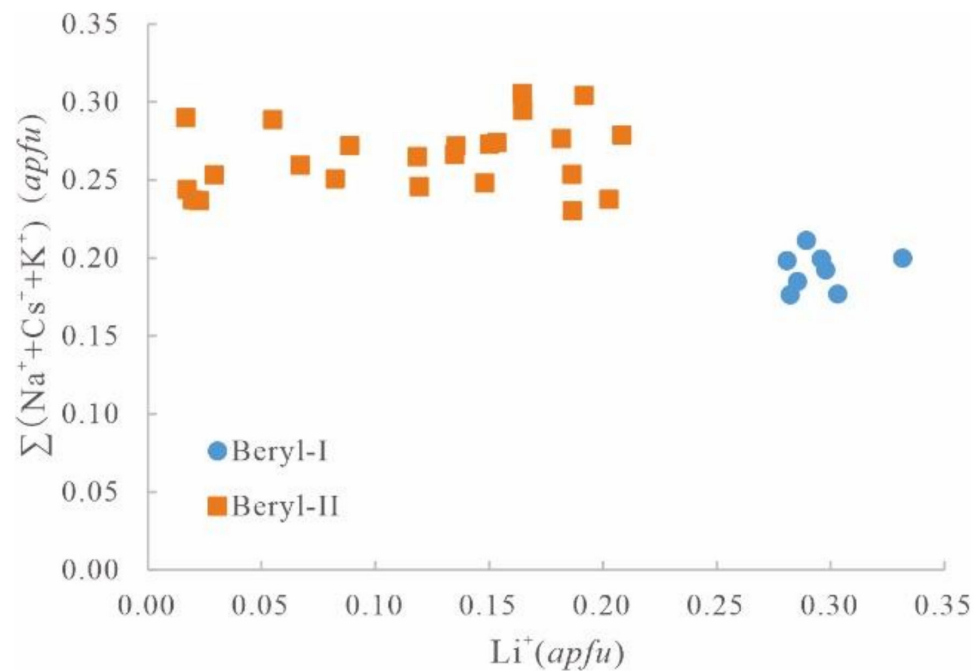
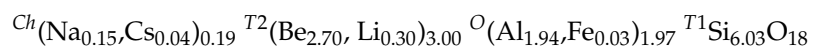


Figure 6. $\text{Li}(\text{apfu})$ vs. $\text{Na} + \text{Cs} + \text{K}(\text{apfu})$ of the beryls from the Xianglin area.

The major, minor and trace elements of beryls from the Xiangling area are listed in Tables 1 and 2. The beryl is essentially composed of SiO_2 , Al_2O_3 , BeO , and some typically minor elements, such as Li_2O , Na_2O , Cs_2O , MgO and FeO (total Fe in the paper). Based on the chemical composition obtained for EPMA and LA-ICP-MS (Tables 1 and 2), the formulas for the two types of beryl from the Xiangling area, using average values of the most important components, are:

(1) Beryl-I (beryl in pegmatite):



(2) Beryl-II (beryl in the hydrothermal veins):



where T^2 and T^1 are the tetrahedral sites for Be and Si, respectively, O is the octahedral site, and Ch is the “channel”.

Table 1. Representative electronic microprobe analysis of beryls from the Xianglin area.

Elt (wt.%)	Beryl-I <i>n</i> = 9						Beryl-II <i>n</i> = 23					
	Max.	Min.	Avg.	CND21-01	CND21-02	CND21-03	Max.	Min.	Avg.	XL20-03	XL20-05	XL20-08
SiO ₂	64.42	63.33	63.72	63.48	63.40	64.10	65.41	63.57	64.33	65.13	65.41	64.25
Al ₂ O ₃	17.63	17.19	17.38	17.26	17.63	17.29	17.43	14.24	15.97	16.61	16.70	15.66
MgO	0.03	0.00	0.01	0.03	0.02	0.01	2.06	1.07	1.62	1.37	1.32	1.66
CaO	0.02	0.00	0.01	0.01	0.00	0.00	0.06	0.00	0.03	0.02	0.01	0.02
FeO	0.59	0.26	0.41	0.48	0.26	0.46	1.31	0.17	0.61	0.23	0.25	0.67
MnO	0.04	0.00	0.01	0.02	0.00	0.01	0.05	0.00	0.01	0.00	0.03	0.00
TiO ₂	0.06	0.00	0.02	0.00	0.00	0.00	0.04	0.00	0.01	0.00	0.01	0.03
Na ₂ O	0.90	0.68	0.81	0.84	0.68	0.90	1.66	1.25	1.43	1.33	1.32	1.25
K ₂ O	0.05	0.02	0.03	0.04	0.03	0.03	0.08	0.01	0.04	0.05	0.02	0.02
Cs ₂ O	1.77	0.31	1.01	1.29	1.77	0.42	0.39	0.00	0.03	0.05	0.00	0.00
Rb ₂ O	0.00	0.00	0.00	0.00	0.00	0.00	0.00	0.00	0.00	0.00	0.00	0.00
Li ₂ O-LA	0.87	0.74	0.78	0.76	0.87	0.75	0.56	0.04	0.31	0.05	0.05	0.49
Li ₂ Ocal	2.48	1.23	1.85	2.18	2.48	1.35	1.73	1.29	1.53	1.45	1.35	1.29
BeOcal	12.05	11.69	11.89	11.88	11.69	11.98	13.55	12.27	12.86	13.51	13.55	12.46
H ₂ Ocal	1.60	1.41	1.52	1.55	1.41	1.60	2.25	1.26	2.00	1.97	1.96	1.90
Total	100.75	96.13	98.24	98.19	98.33	98.04	100.97	98.04	99.56	100.51	100.84	98.60
<i>apfu</i> based on 18 oxygen atoms												
Al ³⁺	1.97	1.92	1.94	1.93	1.97	1.92	1.90	1.60	1.75	1.80	1.80	1.73
Mg ²⁺	0.00	0.00	0.00	0.00	0.00	0.00	0.29	0.15	0.23	0.19	0.18	0.23
Fe ²⁺	0.05	0.02	0.03	0.04	0.02	0.04	0.10	0.01	0.05	0.02	0.02	0.05
Mn ²⁺	0.00	0.00	0.00	0.00	0.00	0.00	0.00	0.00	0.00	0.00	0.00	0.00
Ti ²⁺	0.00	0.00	0.00	0.00	0.00	0.00	0.00	0.00	0.00	0.00	0.00	0.00
ΣO	2.00	1.95	1.97	1.97	2.00	1.96	2.09	1.96	2.03	2.00	2.00	2.02
Ca ²⁺	0.00	0.00	0.00	0.00	0.00	0.00	0.01	0.00	0.00	0.00	0.00	0.00
Na ⁺	0.16	0.12	0.15	0.15	0.12	0.16	0.30	0.23	0.26	0.24	0.23	0.23
K ⁺	0.01	0.00	0.00	0.00	0.00	0.00	0.01	0.00	0.00	0.01	0.00	0.00
Cs ⁺	0.07	0.01	0.04	0.05	0.07	0.02	0.02	0.00	0.00	0.00	0.00	0.00
Rb ⁺	0.00	0.00	0.00	0.00	0.00	0.00	0.00	0.00	0.00	0.00	0.00	0.00
ΣCh	0.21	0.18	0.19	0.21	0.20	0.18	0.31	0.23	0.27	0.25	0.24	0.23
Li ⁺	0.33	0.28	0.30	0.29	0.33	0.29	0.21	0.02	0.12	0.02	0.02	0.19
Be ²⁺	2.72	2.67	2.70	2.71	2.67	2.71	2.98	2.79	2.88	2.98	2.98	2.81
Σ(T2)	3.00	3.00	3.00	3.00	3.00	3.00	3.00	3.00	3.00	3.00	3.00	3.00
Si (T1)	6.05	6.02	6.03	6.03	6.02	6.05	6.08	5.94	6.00	5.99	5.99	6.04

Table 2. Representative trace element compositions of beryls from the Xianglin area, as determined through LA-ICP-MS.

Let (ppm)	Max.	Min.	Avg.	Beryl-I <i>n</i> = 10			Max.	Min.	Avg.	Beryl-II <i>n</i> = 12		
				CND21-01	CND21-02	CND21-03				XL20-05	XL20-06	XL20-07
Li	4253.13	3429.60	3676.10	3519.22	4033.13	3495.12	1106.65	2291.52	207.70	207.70	1913.45	215.32
Be	53,207.23	48,756.05	50,687.47	50,161.02	51,617.32	51,450.77	52,146.64	56,414.49	49,970.46	53,987.71	50,709.42	52,193.78
Rb	215.31	111.98	167.14	215.31	141.68	111.98	147.24	246.53	41.68	240.99	139.45	41.68
Cs	16,734.25	5499.54	10,339.28	5499.54	12,632.12	5587.39	1182.12	2313.76	472.71	1953.34	695.12	472.71
V	3.18	0.00	0.78	0.00	0.94	3.18	36.15	65.95	3.35	18.05	3.35	65.95
Cr	634.58	13.63	136.48	20.24	32.65	243.24	206.25	642.60	17.53	99.31	42.96	59.71
Co	4.96	0.00	0.50	0.00	0.00	0.00	0.64	5.06	0.00	0.00	0.00	1.03
Ni	6.03	0.00	0.91	0.00	6.03	0.00	8.42	65.86	0.00	15.55	65.86	0.00
Cu	18.40	0.00	3.99	0.00	15.78	0.00	20.98	111.86	0.00	0.00	21.39	36.21

Table 2. Cont.

Let (ppm)	Max.	Min.	Avg.	Beryl-I $n = 10$			Max.	Min.	Avg.	Beryl-II $n = 12$		
				CND21-01	CND21-02	CND21-03				XL20-05	XL20-06	XL20-07
Zn	482.89	231.49	396.58	463.16	346.16	231.49	280.30	1781.68	39.63	39.63	188.74	69.41
Ga	41.38	24.32	34.72	37.38	30.41	39.08	43.97	94.94	18.35	94.94	41.31	40.44
As	43.17	0.00	9.63	7.49	6.67	32.09	1511.08	6432.48	0.00	278.44	917.08	6432.48
Sr	1.77	0.00	0.20	1.77	0.00	0.00	2.50	16.88	0.00	0.00	0.00	16.88
Nb	0.33	0.00	0.09	0.14	0.33	0.00	0.13	0.51	0.00	0.00	0.35	0.12
Ta	1.02	0.00	0.14	0.11	0.01	0.00	0.11	0.27	0.00	0.02	0.00	0.10
W	0.15	0.00	0.03	0.00	0.00	0.00	0.08	0.32	0.00	0.00	0.00	0.18
Bi	0.12	0.00	0.03	0.04	0.00	0.04	2.22	9.17	0.00	0.25	2.40	9.17
Pb	2.56	0.00	0.41	0.01	0.09	0.36	1.33	5.00	0.00	0.04	0.03	2.06
Th	1.73	0.00	0.18	0.00	0.00	0.04	2.62	16.46	0.00	0.59	1.79	16.46

A thorough analysis is presented in Sections 5.1 and 5.2.

4.3. LA-ICP-MS Mapping

LA-ICP-MS mapping is used to analyze the complex zonal structure of beryl in the hydrothermal vein of Xianglin area. Judging from the mapping, the complex bands of beryl-II are mainly caused by the difference in the contents of Be, Al, Na, Cs, and Cr (Figure 7).

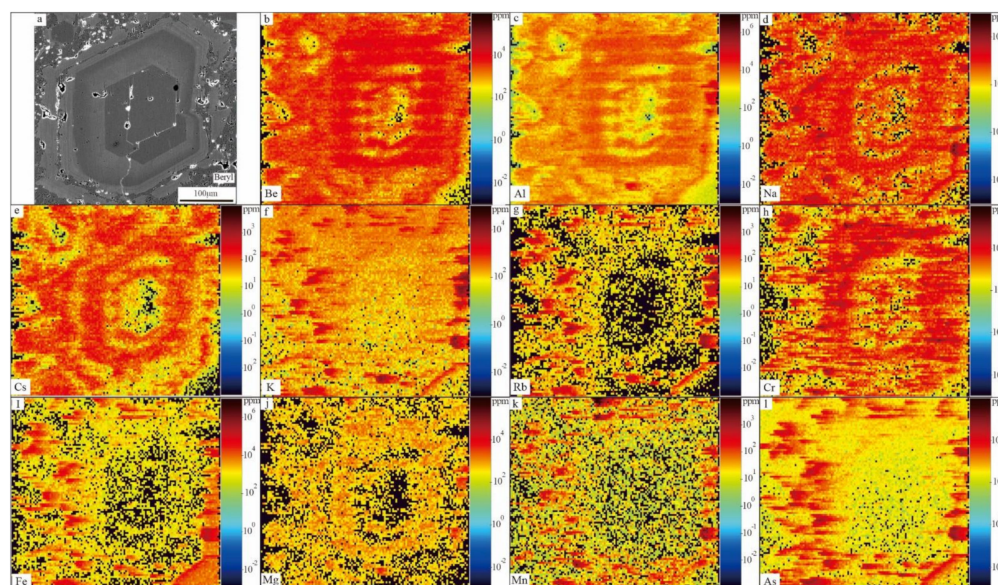


Figure 7. Backscattered electron image (a) and LA-ICP-MS mapping images (b–l) of beryl-II from the hydrothermal vein.

4.4. Unit Cell Parameters

The in situ micro-X-ray diffraction (XRD) analysis results (Table 3) show that the absolute values and average of the unit cell parameter a, b and the c/a ratio have a slight difference between the two types of beryls. Beryl-I has the slightly higher c value (9.2209–9.2243, avg. $c = 9.2228$) and c/a ratio (1.0010–1.0012, avg. 1.0011) than beryl-II ($c = 9.2180$ – 9.2206 , avg. $c = 9.2197$; $c/a = 1.0004$ – 1.0010 , avg. $c/a = 1.0008$).

Table 3. In situ micro-X-ray diffraction (XRD) analysis results of beryls from the Xianglin area.

Sample	<i>a</i> (Å)	<i>b</i> (Å)	<i>c</i> (Å)	<i>V</i> (Å ³)	<i>c/a</i>
CND21-1	9.2103	9.2103	9.2209	677.2920	1.0012
CND21-2	9.2141	9.2141	9.2243	677.9290	1.0011
CND21-3	9.2136	9.2136	9.2231	677.9180	1.0010
Avg.	9.2127	9.2127	9.2228	677.7130	1.0011
Max.	9.2141	9.2141	9.2243	677.9290	1.0012
Min.	9.2103	9.2103	9.2209	677.2920	1.0010
XL20-1	9.2140	9.2140	9.2180	677.7410	1.0004
XL20-2	9.2111	9.2111	9.2202	677.4750	1.0010
XL20-3	9.2139	9.2134	9.2206	677.9130	1.0007
XL20-4	9.2116	9.2130	9.2200	677.7190	1.0009
Avg.	9.2127	9.2129	9.2197	677.7120	1.0008
Max.	9.2140	9.2140	9.2206	677.9130	1.0010
Min.	9.2111	9.2111	9.2180	677.4750	1.0004

5. Discussion

5.1. Crystal Chemical Features

According to the crystallochemical formula of beryl, various cations are incorporated in the beryl structure, resulting in complex substitutions. As divalent cations, such as Fe²⁺ and Mg²⁺, substitute trivalent Al³⁺ in the Y site (octahedral), leading to a charge deficit, the long-radius monovalent cations and divalent cation Ca²⁺ enter the channel to balance the charge [59–64]. Since the Ca²⁺ and K⁺ contents of the two types of beryls from the Xianglin area are negligible (Table 1), the occupying position of Ca²⁺ and K⁺ is not discussed in this paper. The atoms per formula unit of Be²⁺ in the X site of Beryl-I and Beryl-II is 2.70 and 2.89 *apfu*, respectively, showing obvious unsaturation. Li⁺ is the main substitute cation in the X site, and the atoms per formula unit are 0.30 and 0.11 *apfu*, respectively, indicating that the replacement degree of the X site ion of Beryl-I is higher than that of Beryl-II. The atoms per formula unit of Al³⁺ in the Y site of Beryl-I is 1.94 *apfu*, and the isomorphic substitution is 0.03 *apfu*, manifesting that the substitution degree of the Y site of Beryl-I is low, whereas the atoms per formula unit of Al³⁺ is 1.76 *apfu*, and the substitution of the Y site is 0.27 *apfu*, indicating that the substitution degree of the Y site of Beryl-II is relatively higher than that of Beryl-I.

Ideally, the sum of divalent cations in the Y site (R²⁺) and monovalent alkali cations in channel (A⁺) of beryl is close to 1:1 [65]. It can be illustrated with Figure 8 that all the points of Beryl-I lie at a high position above the 1:1 slope line, showing an obvious substitution in the channel. The points of Beryl-II are mostly located near the slope of R²⁺ = A⁺, and some points lie at a high position above the slope, indicating a certain amount of A⁺ entering the X and Y sites.

Linear fitting is performed on the main cation contents of the two types of beryl at the X site, Y site and channel (Figure 9). In Beryl-I, the negative correlation between Li and Na, Li and Cs, Na and Cs, and Fe and Al indicates that the mechanism of element substitution in Beryl-I includes (Na,Cs)Li□₁Be₁ channel-tetrahedral substitution, (Na,Cs)Fe²⁺□₁Al₁ channel-octahedral substitution and NaCs₁ the mutual substitution of alkali metal ions in the “channel”. By comparison, in Beryl-II, Na and Li are weakly negatively correlated, Al is negatively correlated with Mg + Fe²⁺, Mg, Fe²⁺, and Mg is also negatively correlated with Fe²⁺, which can be inferred that the element substitution mechanism of Beryl-II is composed of NaLi□₁Be₁ channel-tetrahedral substitution and Na(Fe²⁺,Mg)□₁Al₁ channel-octahedral substitution.

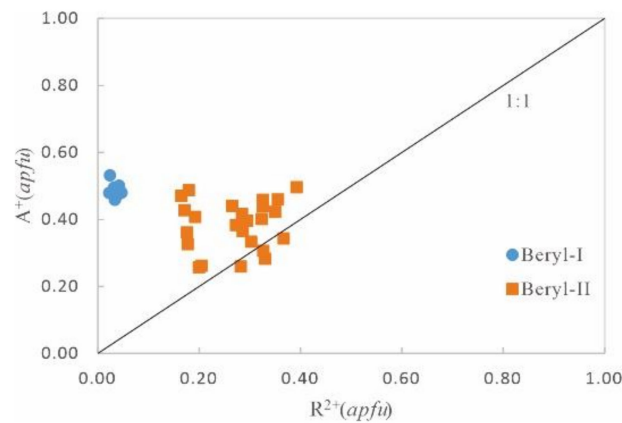


Figure 8. Plot of R^{2+} versus A^+ . R^{2+} represents divalent cations in the Y (octahedral) site, including Fe, Mg; A^+ represents monovalent alkali cations in the channel, including Na, Cs.

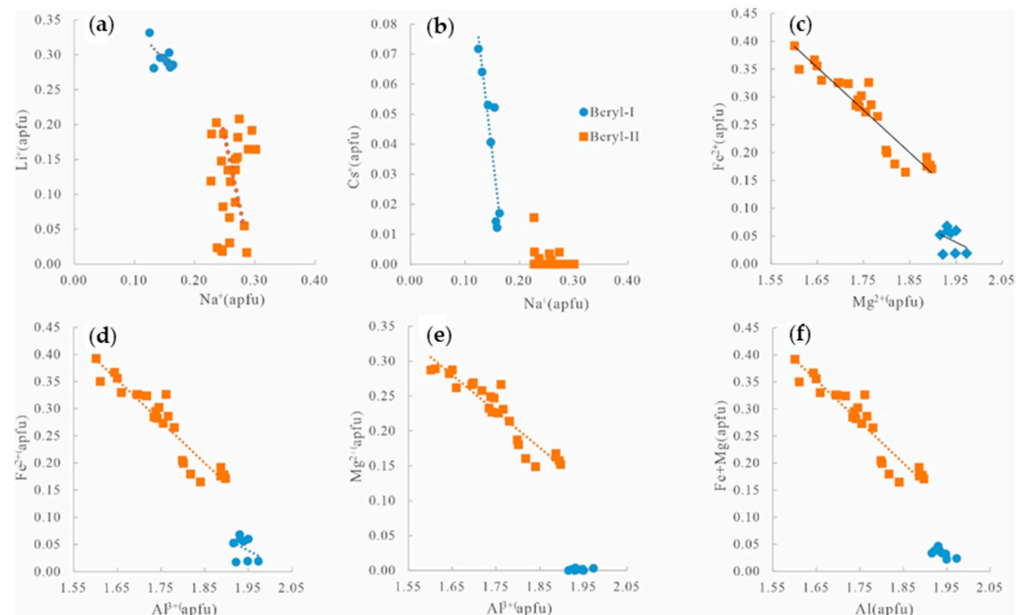


Figure 9. Plots of main cations in the X site, Y site and channel of beryl. (a): Li^+ vs. Na^+ plot. (b): Cs^+ vs. Na^+ plot. (c): Fe^{2+} vs. Mg^{2+} plot. (d): Fe^{2+} vs. Al^{3+} plot. (e): Mg^{2+} vs. Al^{3+} plot. (f): $(Fe^{2+} + Mg^{2+})$ vs. Al^{3+} plot. Fe is one of the most important chromogenic ions of beryl. In addition to replacing Al^{3+} in the Y (octahedral) site, Fe appears in the channel, making it appear light green, blue–green, green–blue and light blue [56]. Emerald is chromitized by Fe, V and Cr [59], and a certain amount of Fe, V and Cr is detected in Beryl-I and Beryl-II. Thereby, there is likely to be a potential for further emerald prospecting at the Xianglin area.

5.2. Classification

As the ions are replaced, the unit cell parameters of the minerals also change. Based on the difference in the ratio of c/a , beryl is divided into three types: ① n-beryl (normal beryl, $c/a = 0.997\sim 0.998$), ideal pure beryl without replacement; ② o-beryl (octahedral beryl, $c/a = 0.991\sim 0.996$), of which Al^{3+} in the center is partially replaced; ③ t-beryl (tetrahedral beryl, $c/a = 0.999\sim 1.003$), of which a large number of metal ions enter the structure channel to balance the electricity price [4]. The c/a ratios of Beryl-I and Beryl-II from the Xianglin area range from 1.0004 to 1.0012 (Table 3), which shows that the beryls from the Xianglin area are t-beryl. Significantly, the c/a ratios of Beryl-I and -II show a slight decreasing trend, which is probably caused by the accommodation of alkali elements and substitution of Be^{2+} and Li^+ in the beryl structure along the c -axis [66]. It may reflect the hydrothermal process in the late stage of pegmatite evolution [9,10].

According to the contents of alkali metal elements, beryl can be classified into five types [3]: (1) alkali-free beryl (total $R_2O < 0.5$ wt%, where $R = Na, Li, Cs, K$); (2) alkali beryl (total $R_2O > 0.5$ wt%); (3) Na beryl (total $R_2O > 0.5$ wt%, $Na_2O = 0.5\text{--}2$ wt%, $Li_2O = 0.1\text{--}0.5$ wt%); (4) Na–Li beryl ($Li_2O = 0.5\text{--}1.5$ wt% and $Na_2O = 1\text{--}2.5$ wt%); and (5) Li–Cs beryl ($Li_2O = 0.1\text{--}1$ wt%, $Cs_2O < 3$ wt%, $Na_2O = 0.3\text{--}1$ wt%). Therefore, the beryls at the Xianglin area are alkali beryls, of which beryl-I is Li–Cs beryl, with $R_2O = 1.97\text{--}3.35$ wt%, $Na_2O = 0.68\text{--}0.90$ wt%, $Li_2O = 0.74\text{--}0.87$ wt%, $Cs_2O = 0.31\text{--}1.77$ wt% (Figure 10a); while beryl-II consists of Na and Na–Li beryl, with $R_2O = 1.40\text{--}2.20$ wt%, $Na_2O = 1.25\text{--}1.66$ wt%, $Li_2O = 0.04\text{--}0.56$ wt%, $Cs_2O = 0.00\text{--}0.39$ wt% (Figure 10b).

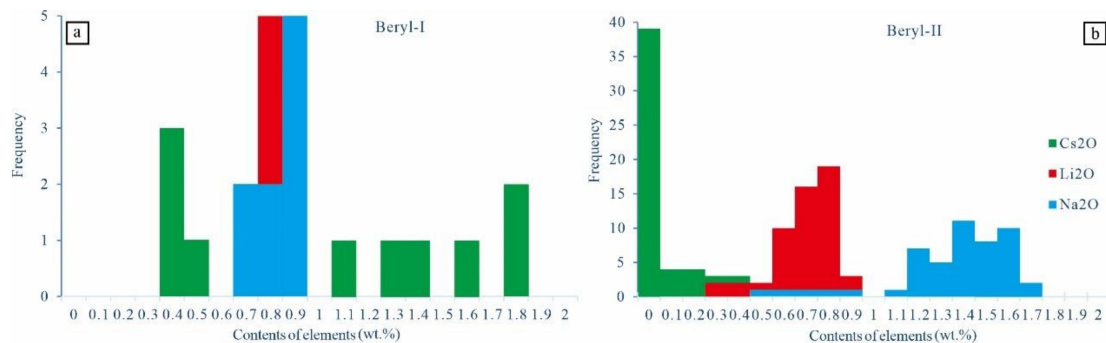


Figure 10. Frequency histogram of alkali elements of beryl from the Xianglin area. (a): Alkali elements of Beryl-I. (b): Alkali elements of Beryl-II.

Furthermore, the contents of alkali metal elements can indicate the magmatic–hydrothermal evolution trend of granitic pegmatite [67]; that is, the increasing content of Cs and Cs/Na ratio of beryl has been identified as the process of evolution and differentiation of pegmatite from low to high, with the possibility of decreasing content of Mg and Mg/Fe ratio. The high Mg/Fe ratio is generally considered to be affected by hydrothermal alkali-metasomatism [8,34].

Judging from the plot of Mg/Fe vs. Cs/Na (Figure 11), there are obvious evolutionary differences between the two beryls. The content of Cs₂O of beryl-I in pegmatite ranges from 0.31 to 1.77 wt% (avg. = 1.01 wt%), and the ratio of Cs/Na (apfu) = 0.10–0.44 (avg. = 0.28), with almost no MgO detected. It is indicated that beryl-I was formed under highly differentiated evolution conditions [4]. By contrast, the content of MgO in beryl-II is higher, ranging from 0.46 to 2.25 wt%, avg. = 1.48 wt%, and the ratio of Mg/Fe (apfu) ranging from 2.73 to 17.31, avg. = 6.33, with the low content of Cs₂O inferring that Beryl-II probably experienced hydrothermal alkali-metasomatism [10].

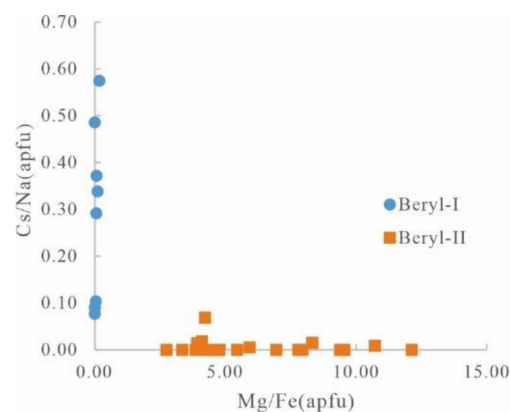


Figure 11. Mg/Fe vs. Cs/Na diagram of beryl from the Xianglin area.

5.3. Metallogenic Mechanism

The solution and saturation of beryllium in granitic magma are mainly controlled by five factors [4–7]: temperature, pressure, melt composition, fractionation, and the volatile components such as B, P, and F.

The geological characteristics, metallogenic chronology, stable isotopes and fluid inclusions of the Cuonadong Be-Sn-W polymetallic deposit show that the ore-forming materials and fluids of the deposit are derived from Cuonadong leucogranite [14–24]. Cuonadong leucogranite, a typical representative of the Himalayan leucogranite belt, is a complex pluton formed by the multi-stage evolution of homologous magma, including the early strongly deformed two-mica granite, the middle weakly deformed two-mica leucogranite and the late undeformed muscovite leucogranite, of which the chemical composition gradually evolved to be of higher silicon, more alkalis and more volatile [19–24]. Beryllium, an incompatible element, would preferentially enter the melt phase during the differentiation and evolution of magma. With the continuous process of this interaction, volatile compounds and ore-forming fluids can often be released from the late magmatism [68]. Highly differentiated leucogranites generally have a high alumina saturation index (ASI), of which beryllium content is positively proportional to ASI value [5,69]. In addition, the beryllium content has a weak to moderate negative correlation with the potassium content, and the reduction of potassium is due to the homogeneous reaction of volatile anions such as F, P, and B with the Na-containing magmatic melt [5]. That is, the more potassium phases (e.g., K-feldspar, mica) that gradually dominate the crystallization mode, the more sodium remains in the melt [70]. Flux components (F, B, P) in pegmatite melts can form some stable fluoride, borate and phosphate migration with rare metals [4,71]; thereby, the transitional fluids with the coexistence of magmatic fluid and residual magma, rich in Be, Sn, W, B, F, H₂O, migrate to the top of the granitic or surrounding rocks [72] (Figure 12). Due to the intrusion of pegmatite magma into the surrounding rock, there is a significant temperature difference between the two, resulting in undercooling of the melt-liquid phase and a decrease in the solubility of rare metal minerals [69]. Meanwhile, some minerals rich in flux components (such as fluorite, tourmaline, and apatite) crystallize [73], leading to a great decrease in contents of flux components such as F, B, and P in the ore-forming system and Beryl-I crystallization. It is also the reason why Beryl-I is mainly produced in the contact between albitite pegmatite and the surrounding rock.

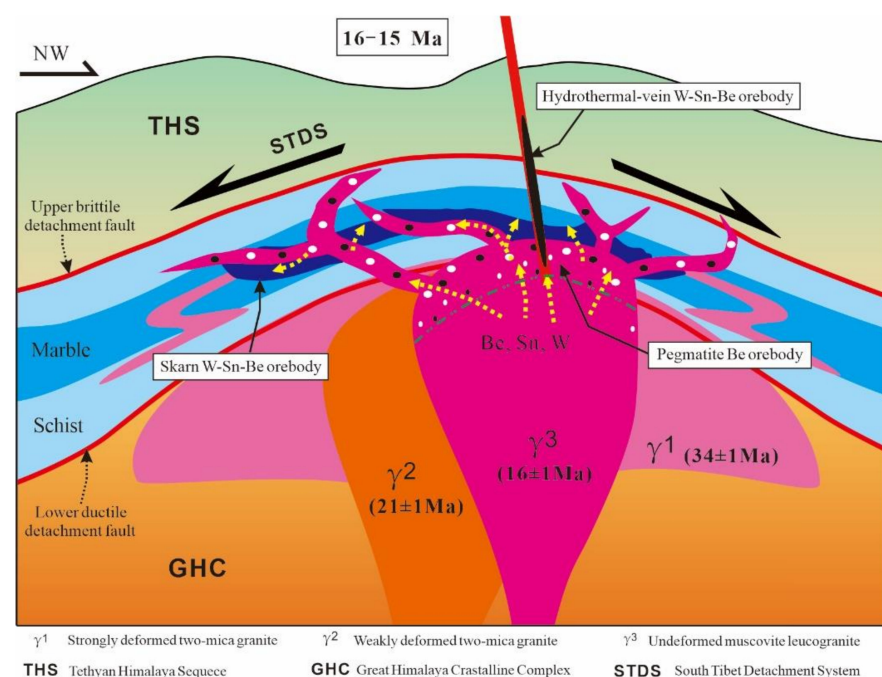
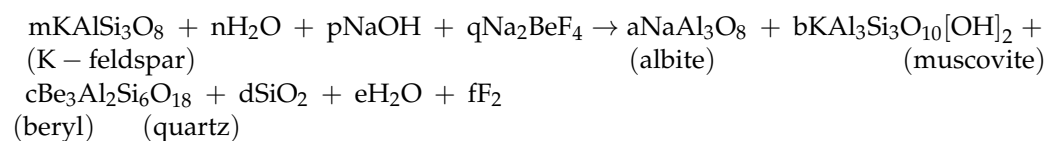


Figure 12. Metallogenic model of the Cuonadong deposit, Tibet (after [72]).

With the continuous differentiation and crystallization of the leucogranitic magma, a large number of ore-forming materials such as Be, W and Sn are brought out. When the ore-bearing fluid migrates to the marble layer with pressure releasing, extensive water–rock reactions occur between the ore-bearing fluid and marble layer [72], and then the skarn be-W-Sn ore body is formed (Figure 12). Beryllium mainly occurs in skarn minerals such as vesuvianite, scapolite and garnet modified by late hydrothermal solution, in the form of isomorphisms [32].

Influenced by the east–west extensional structure, some nearly north–south normal faults and secondary faults were developed in the middle Miocene (16–15 Ma) [27]. Ore-forming fluids migrated along these faults, and with the decrease in temperature and the mixing of some hydrothermal water, the hydrothermal vein-type Be-Sn-W ore (chemical) bodies were formed [72] (Figure 12). It can be seen from the above discussion (Section 5.2) that beryl in hydrothermal vein-type ore bodies is related to hydrothermal activity. The microthermometry results of fluid inclusions show that the temperature of ore-forming fluid of hydrothermal vein orebodies ranges from 197 to 343 °C [28]. Under such mineralization conditions, beryllium mostly exists in the form of fluoride, chloride, and complexes containing fluorine or chlorine, while beryllium tends to migrate as beryllium carbonate complexes if the activity of fluorine in the solution is low and the activity of carbonic acid is high [74,75]. There are many wide fluorite veins in the Cuonadong mining area [17,28], indicating that the ore-forming fluid is extremely rich in fluorine. Therefore, it can be inferred that beryllium is most likely transported as beryllium fluoride (BeF) or fluoride complex ions (e.g., $[\text{BeF}_4]^{2-}$) [74], in this area. The result of beryl-II's mapping shows that the development of these complex zonings is mainly caused by the differences among the contents of elements such as Na, Cs, Be, Al, Cr, and As (Figure 7). It probably reflects the unbalanced crystallization environment and the heterogeneity of ore-forming fluids, indicating that extensive fluid immiscibility and metasomatism has occurred in the metallogenic system [72], and it has undergone the superimposed transformation of later ore-forming fluids, such as strong alkaline metasomatism in the late period of beryl mineralization [10,76]. Field geological survey studies have shown that a variety of alterations, such as greisenization and albitization, often develop in the hydrothermal vein orebodies [77]. During the process, liquid H_2O is bound to be generated, which cannot only reduce the temperature, but can also react with beryllium complexes in the ore-forming fluid and combine with Si and Al, thereby forming hydrothermal beryl. The probable reaction formula is as follows [77]:



Beryl occurrences in the pegmatites and hydrothermal vein ore bodies in the Cuonadong mining area indicate that beryllium mineralization is characterized by magmatic–hydrothermal transition. Some granitic rare metal deposits in South China have similar characteristics; that is, the pegmatic crusts usually develop on the top of the granitic rock mass, while hydrothermal mineralization occurs at the surroundings of the rock mass, and the hydrothermal mineralization pattern is closely related to the surrounding rocks [10,78,79]. A large number of leucogranites similar to the Cuonadong leucogranite are developed in the Himalayas, and the Tethys Himalayan sedimentary sequence is mainly a set of clastic rocks and carbonate rocks originating from passive Indian continental margin [32]. In conclusion, there is further great potential and prospects for the pegmatite, skarn and hydrothermal-vein rare metal deposits related to leucogranite in the Himalayas.

6. Conclusions

The results of this study allow for the following conclusions for beryls from the Cuonadong deposit.

- (1) In terms of composition, beryls in the Cuonadong deposit are alkaline beryls, among which beryl-I is Li-Cs beryl, and beryl-II consists of Na and Na-Li beryl. Structurally, they are *t*-beryls. This indicates that beryl has experienced magmatism to hydrothermal alkali-metasomatism in the late stage of pegmatitic magmatism during formation.
- (2) The mechanism of element substitution in Beryl-I includes (Na,Cs)Li \square_{-1} Be \square_{-1} channel-tetrahedral substitution, (Na,Cs)Fe $^{2+}$ \square_{-1} Al \square_{-1} channel-octahedral substitution and NaCs \square_{-1} the mutual substitution of alkali metal ions in the “channel”, whereas that in Beryl-II consists of NaLi \square_{-1} Be \square_{-1} channel-tetrahedral substitution and Na(Fe $^{2+}$,Mg) \square_{-1} Al \square_{-1} channel-octahedral substitution.
- (3) The precipitation of Beryl-I is mostly caused by the emplacement of highly fractionated magma containing Be to the top of the rock mass or surrounding rock, the melt-fluid undercooling, and the crystallization of volatile minerals (such as tourmaline and fluorite).
- (4) Beryl-II precipitates owe to the ore-forming fluid mixing with the hydrothermal water and cooling and large amounts of crystallization of volatile minerals (mainly fluorite).

Author Contributions: Y.W.: Investigation, Conceptualization, Supervision, Formal Analysis, Writing—Original Draft, Writing—Review and Editing. G.L.: Investigation, Formal Analysis, Funding Acquisition. W.L.: Investigation, Resources. Z.Z.: Formal Analysis, Data Curation. All authors have read and agreed to the published version of the manuscript.

Funding: This work was sponsored by the National Key R&D Program of China (2019YFC0605201) and the National Natural Science Foundation of China (91955208 and 42002097).

Data Availability Statement: All data derived from this research are presented in the enclosed figures and tables.

Acknowledgments: The authors appreciate two anonymous reviewers for the scientific suggestions and Zhen-Yu Chen at the Chinese Academy of Geological Sciences and Li-Min Zhou at the National Research Center for Geoanalysis for their laboratory assistance and thoughtful discussions. This work also benefited from helpful discussions with Yong Huang, Jian-Gang Fu, Anping Xiang, Cheng-Shi Qing, Jian-Yang Wu, Li Ying-Xu, Guo-Tao Ma, Lei Dong, and Ke Gao.

Conflicts of Interest: The authors declare no conflict of interest.

References

1. London, D.; Evensen, J.M. Beryllium in silicic magmas and the origin of beryl-bearing pegmatites. *Rev. Mineral. Geochem.* **2002**, *50*, 445–485. [\[CrossRef\]](#)
2. Evensen, J.M.; London, D. Experimental partitioning of Be, Cs, and other trace elements between cordierite and felsic melt, and the chemical signature of S-type granite. *Contrib. Mineral. Petrol.* **2003**, *144*, 739–757. [\[CrossRef\]](#)
3. Černý, P. Alkali variations in pegmatitic beryls and their petrogenetic implications. *Neues Jahrb. Mineral. Abh.* **1975**, *123*, 198–212.
4. Charoy, B. Beryllium speciation in evolved granitic magmas: Phosphates versus silicates. *Eur. J. Mineral.* **1999**, *11*, 135–148. [\[CrossRef\]](#)
5. Evensen, J.M.; London, D.; Wendlandt, R.F. Solubility and stability of beryl in granitic melts. *Am. Mineral.* **1999**, *84*, 733–745. [\[CrossRef\]](#)
6. London, D. Reading Pegmatites: Part 1—What Beryl Says. *Rocks Min.* **2015**, *90*, 138–153. [\[CrossRef\]](#)
7. Barton, M.D.; Young, S. Non-pegmatitic Deposits of Beryllium: Mineralogy, Geology, Phase Equilibria and Origin. *Rev. Mineral. Geochem.* **2002**, *50*, 591–691. [\[CrossRef\]](#)
8. Zhou, Q.F.; Qin, K.Z.; Tang, D.M.; Wang, C.L.; Ma, L.S. Mineralogical characteristics and significance of beryl from the rare-element pegmatites in the Lushi County, East Qinling, China. *Acta Petrol. Sin.* **2019**, *35*, 1999–2012.
9. Černý, P.; Anderson, A.J.; Tomascak, P.B.; Chapman, R. Geochemical and morphological features of beryl from the Bikita granitic pegmatite, Zimbabwe. *Can. Mineral.* **2003**, *41*, 1003–1011. [\[CrossRef\]](#)
10. Wang, R.C.; Che, X.D.; Zhang, W.L.; Zhang, A.C.; Zhang, H. Geochemical evolution and late re-equilibration of Na-Cs-rich beryl from the Koktokay #3 pegmatite (Altai, NW China). *Eur. J. Mineral.* **2009**, *21*, 795–809.
11. Zhou, Q.; Qin, K.; Tang, D.; Wang, C.; Tian, Y.; Sakyi, P.A. Mineralogy of the Koktokay No.3 Pegmatite, Altai, NW China: Implications for Evolution and Melt-Fluid Processes of Rare-metal pegmatites. *Eur. J. Mineral.* **2015**, *27*, 433–457. [\[CrossRef\]](#)
12. Bragg, W.L.; West, J. The structure of beryl, Be $_3$ Al $_2$ Si $_6$ O $_{18}$. *Proc. R. Soc. London. Ser. A Contain. Pap. Math. Phys. Character.* **1926**, *111*, 691–714.

13. Gibbs, G.V.; Breck, D.W.; Meagher, E.P. Structural refinement of hydrous and anhydrous synthetic beryl, $\text{Al}_2(\text{Be}_3\text{Si}_6)\text{O}_{18}$ and emerald, $\text{Al}_{1.9}\text{Cr}_{0.1}(\text{Be}_3\text{Si}_6)\text{O}_{18}$. *Lithos* **1968**, *1*, 275–285. [[CrossRef](#)]
14. Li, G.M.; Zhang, L.K.; Jiao, Y.J.; Xia, X.B.; Dong, S.L.; Fu, J.G.; Liang, W.; Zhang, Z.; Wu, J.Y.; Dong, L.; et al. First discovery and implications of Cuonadong superlarge Be-W-Sn polymetallic deposit in Himalayan metallogenic belt, southern Tibet. *Miner. Depos.* **2017**, *36*, 1003–1008.
15. Zhang, Z.; Zhang, L.K.; Li, G.M.; Liang, W.; Xia, X.B.; Fu, J.G.; Dong, S.L.; Ma, G.T. The Cuonadong Gneiss Dome of North Himalaya: A New Member of Gneiss Dome and a New Proposition for the Ore-controlling Role of North Himalaya Gneiss Domes. *Acta Petrol. Sin.* **2017**, *38*, 754–766.
16. Liang, W.; Zhang, L.K.; Xia, X.B.; Ma, G.T.; Huang, Y.; Zhang, Z.; Fu, J.G.; Cao, H.W.; Miao, H.Q.; Li, G.M. Geology and preliminary mineral genesis of the Cuonadong W-Sn polymetallic deposit, Southern Tibet, China. *Earth Sci.* **2018**, *43*, 2742–2754.
17. Xia, X.B.; Li, G.M.; Zhang, L.K.; Zhang, Z.; Cao, H.W.; Liang, W. Geological characteristics of and prospecting strategy for the Xianglin Be-Sn polymetallic ore deposit in the Cuonadong gneiss dome in southern Tibet. *Earth Sci. Front.* **2022**, *29*, 93–106.
18. Gao, L.E.; Gao, J.H.; Zhao, L.H.; Hou, K.J.; Tang, S.H. The Miocene leucogranite in the Nariyongcuo gneiss dome, southern Tibet: Products from melting metapelite and fractional crystallization. *Acta Petrol. Sin.* **2017**, *33*, 2395–2411.
19. Zhang, L.K.; Zhang, Z.; Li, G.M.; Dong, S.L.; Xia, X.B.; Liang, W.; Fu, J.G.; Cao, H.W. Rock Assemblage, Structural Characteristics and Genesis Mechanism of the Cuonadong Dome, Tethys Himalaya. *Earth Sci.* **2018**, *43*, 2664–2683.
20. Dong, H.W.; Xu, Z.Q.; Meng, Y.K.; Yi, Z.Y. Geochronology of leucogranites in the Cuonadong dome, southern Tibet and limitation of the timing of the Southern Tibet detachment System (STDS). *Acta Petrol. Sin.* **2017**, *33*, 3741–3752.
21. Fu, J.G.; Li, G.M.; Wang, G.H.; Zhang, L.K.; Liang, W.; Zhang, Z.; Dong, S.L.; Huang, Y. Timing of E-W extension deformation in North Himalaya: Evidences from ArAr age in the Cuonadong dome, South Tibet. *Earth Sci.* **2018**, *43*, 2638–2650.
22. Fu, J.G.; Li, G.M.; Wang, G.H.; Zhang, L.K.; Liang, W.; Zhang, Z.; Zhang, X.Q.; Huang, Y. Synchronous granite intrusion and E-W extension in the Cuonadong dome, southern Tibet, China: Evidence from field observations and thermochronologic results. *Int. J. Earth Sci.* **2018**, *107*, 2023–2041. [[CrossRef](#)]
23. Fu, J.; Li, G.; Wang, G.; Zhang, L.; Liang, W.; Zhang, X.; Jiao, Y.; Dong, S.; Huang, Y. Structural analysis of sheath folds and geochronology in the Cuonadong Dome, southern Tibet, China: New constraints on the timing of the South Tibetan Detachment System and its relationship to North Himalayan Gneiss Domes. *Terra Nova* **2020**, *32*, 300–323. [[CrossRef](#)]
24. Xie, L.; Qiu, H.; Bai, X.; Zhang, W.; Wang, Q.; Xia, X. Geochronological and geochemical constraints on the Cuonadong leucogranite, eastern Himalaya. *Acta Geochim.* **2018**, *37*, 347–359. [[CrossRef](#)]
25. Xia, X.B.; Li, G.M.; Cao, H.W.; Liang, W.; Fu, J.G. Petrogenic Age and Geochemical Characteristics of the Mother Rock of Skarn Type Ore Body in the Cuonadong Be-W-Sn Polymetallic Deposit, Southern Tibet. *Earth Sci.* **2019**, *44*, 2207–2223.
26. Xia, X.B.; Xiang, A.P.; Li, G.M.; Zhang, L.K.; Cao, H.W.; Zhang, Z.; Liang, W. Neoproterozoic magmatism of Cuonadong dome and its tectonic implication, Tibet, China. *J. Chengdu Univ. Technol. (Sci. Technol. Ed.)* **2019**, *46*, 435–448.
27. Cao, H.W.; Li, G.M.; Zhang, Z.; Zhang, L.K.; Dong, S.L.; Xia, X.B.; Liang, W.; Fu, J.G.; Huang, Y.; Xiang, A.P.; et al. Miocene Sn polymetallic mineralization in the Tethyan Himalaya, southeastern Tibet: A case study of the Cuonadong deposit. *Ore Geol. Rev.* **2020**, *119*, 103403. [[CrossRef](#)]
28. Cao, H.W.; Li, G.M.; Zhang, R.Q.; Zhang, Y.H.; Zhang, L.K.; Dai, Z.W.; Zhang, Z.; Liang, W.; Dong, S.L.; Xia, X.B. Genesis of the Cuonadong tin polymetallic deposit in the Tethyan Himalaya: Evidence from geology, geochronology, fluid inclusions and multiple isotopes. *Gondwana Res.* **2021**, *92*, 72–101. [[CrossRef](#)]
29. Liang, W.; Li, G.M.; Zhang, L.K.; Fu, J.G.; Huang, Y.; Zhang, Z. Cuonadong Be-rare polymetallic metal deposit: Constraints from Ar-Ar age of hydrothermal muscovite. *Sediment. Geol. Tethyan Geol.* **2020**, *40*, 76–81.
30. Lin, B.; Tang, J.X.; Zheng, W.B.; Leng, Q.F.; Lin, X.; Wang, Y.Y.; Meng, Z.; Tang, P.; Ding, S.; Xu, Y.F.; et al. Geochemical characteristics, age and genesis of Cuonadong leucogranite, Tibet. *Acta Petrol. Miner.* **2016**, *35*, 391–406.
31. Huang, C.M. Petrogenesis of the Cuonadong-Lhozag Leucogranites and Implication for Tectonic Evolution and Be-W-Sn Metallogeny in Southern Tibet. Ph.D. Thesis, China University of Geosciences, Beijing, China, 2019.
32. He, C.T.; Qin, K.Z.; Li, J.X.; Zhou, Q.F.; Zhao, J.X.; Li, G.M. Preliminary study on occurrence status of beryllium and genetic mechanism in Cuonadong tungsten-tin-beryllium deposit, eastern Himalaya. *Acta Petrol. Sin.* **2020**, *36*, 3593–3606.
33. Shen, J.Q.; Hu, Z.K.; Cui, S.Y.; Zhang, Y.F.; Li, E.Q.; Liang, W.; Xu, B. A Study on Beryl in the Cuonadong Be-W-Sn Polymetallic Deposit, Longzi County, Tibet, China. *Crystals* **2021**, *11*, 777. [[CrossRef](#)]
34. Tao, X.Y.; Xie, L.; Wang, R.C.; Zhang, R.Q.; Hu, H.; Liu, C. Mineralogical characteristics of beryl: A case study of the beryls from Cuona and Qomolangma district in Himalaya. *J. Nanjing Univ. (Nat. Sci.)* **2020**, *56*, 815–829.
35. Burchfiel, B.C.; Chen, Z.; Hodges, K.V.; Liu, Y.; Royden, L.H.; Deng, C.; Xu, J. The south Tibetan detachment system, Himalayan orogen: Extension contemporaneous with and parallel to shortening in a collisional mountain belt. *Geol. Soc. Am. Spec. Pap.* **1992**, *269*, 1–41.
36. Pan, G.T.; Wang, L.Q.; Li, R.S.; Yuan, S.H.; Ji, W.H.; Yin, F.G.; Zhang, W.P.; Wang, B.D. Tectonic evolution of the Qinghai-Tibet Plateau. *J. Asian Earth Sci.* **2012**, *53*, 3–14. [[CrossRef](#)]
37. Burg, J.-P.; Bouilhol, P. Timeline of the South-Tibet-Himalayan belt: The geochronological record of subduction, collision, and underthrusting from zircon and monazite U-Pb ages. *Can. J. Earth Sci.* **2019**, *56*, 1318–1332. [[CrossRef](#)]
38. Yin, A.; Harrison, T.M. Geologic evolution of the Himalayan-Tibetan orogen. *Annu. Rev. Earth Planet. Sci.* **2000**, *28*, 211–280. [[CrossRef](#)]

39. Yang, Z.S.; Hou, Z.Q.; Meng, X.J.; Liu, Y.C.; Fei, H.C.; Tian, S.H.; Li, Z.Q.; Gao, W. Post-collisional Sb and Au mineralization related to the South Tibetan detachment system, Himalayan orogen. *Ore Geol. Rev.* **2009**, *36*, 194–212. [[CrossRef](#)]
40. Zhai, W.; Sun, X.; Yi, J.; Zhang, X.; Mo, R.; Zhou, F.; Wei, H.; Zeng, Q. Geology, geochemistry, and genesis of orogenic gold–antimony mineralization in the Himalayan Orogen, South Tibet, China. *Ore Geol. Rev.* **2014**, *58*, 68–90. [[CrossRef](#)]
41. Hou, Z.Q.; Zhang, H.R. Geodynamics and metallogeny of the eastern Tethyan metallogenic domain. *Ore Geol. Rev.* **2015**, *70*, 346–384. [[CrossRef](#)]
42. Sun, X.M.; Wei, H.X.; Zhai, W.; Shi, G.Y.; Liang, Y.H.; Mo, R.W.; Han, M.X.; Yi, J.Z.; Zhang, X.G. Fluid inclusion geochemistry and Ar–Ar geochronology of the Cenozoic Bangbu orogenic gold deposit, southern Tibet, China. *Ore Geol. Rev.* **2016**, *74*, 196–210. [[CrossRef](#)]
43. Wang, D.; Zheng, Y.; Mathur, R.; Jiang, J.; Zhang, S.; Zhang, J.; Yu, M. Multiple mineralization events in the Zhaxikang Sb–Pb–Zn–Ag deposit and their relationship with geodynamic evolution in the North Himalayan Metallogenic Belt, South Tibet. *Ore Geol. Rev.* **2019**, *105*, 201–215. [[CrossRef](#)]
44. Liu, C.; Wang, R.C.; Wu, F.Y.; Xie, L.; Liu, X.C.; Li, X.K.; Yang, L.; Li, X.J. Spodumene pegmatites from the Pusila pluton in the higher Himalaya, South Tibet: Lithium mineralization in a highly fractionated leucogranite batholith. *Lithos* **2020**, *358–359*, 105421. [[CrossRef](#)]
45. Visonà, D.; Lombardo, B. Two mica and tourmaline leucogranites from the Everest-Makalu region (NepalTibet). Himalayan leucogranite genesis by isobaric heating? *Lithos* **2002**, *62*, 125–150. [[CrossRef](#)]
46. Xie, L.; Tao, X.Y.; Wang, R.C. Highly fractionated leucogranites in the eastern Himalayan Cuonadong dome and related magmatic Be–Nb–Ta and hydrothermal Be–W–Sn mineralization. *Lithos* **2020**, *354–355*, 105286. [[CrossRef](#)]
47. Wang, R.C.; Wu, F.Y.; Xie, L.; Liu, X.C.; Wang, J.M.; Yang, L.; Lai, W.; Liu, C. A preliminary study of rare-metal mineralization in the Himalayan leucogranite belts, South Tibet. *China Earth Sci.* **2017**, *60*, 1655–1663. [[CrossRef](#)]
48. Wu, F.Y.; Liu, X.C.; Liu, Z.C.; Wang, R.C.; Xie, L.; Wang, J.M.; Ji, W.Q.; Yang, L.; Liu, C.; Khanal, G.P.; et al. Highly fractionated Himalayan leucogranites and associated rare-metal mineralization. *Lithos* **2020**, *352–353*, 105319. [[CrossRef](#)]
49. Wu, F.Y.; Wang, R.C.; Liu, X.C.; Xie, L. New breakthroughs in the studies of Himalayan rare-metal mineralization. *Acta Petrol. Sin.* **2021**, *37*, 3261–3276.
50. Zhang, Z.; Li, G.M.; Zhang, L.K.; Dong, S.L.; Liang, W.; Fu, J.G.; Huang, Y.; Cao, H.W.; Xia, X.B. The early Oligocene beryl-bearing pegmatite in the Cuonadong dome, southern Tibet: Its forming mechanism and geological significances. *Sedimentary Geol. Tethyan Geol.* **2020**, *40*, 14–30.
51. Li, G.M.; Zhang, L.K.; Zhang, Z.; Xia, X.B.; Liang, W.; Hou, C.Q. New exploration progresses, resource potentials and prospecting targets of strategic minerals in the southern Qinghai-Tibet Plateau. *Sedimentary Geol. Tethyan Geol.* **2021**, *41*, 351–360.
52. Tunheng, A.; Hirata, T. Development of signal smoothing device for precise elemental analysis using laser ablation-ICP-mass spectrometry. *J. Anal. At. Spectrom.* **2004**, *19*, 932–934. [[CrossRef](#)]
53. Liu, S.B.; Wang, D.H.; Chen, Y.C.; Li, J.K.; Ying, L.J.; Xu, J.X.; Zeng, Z.L. ⁴⁰Ar/³⁹Ar ages of muscovite from different types tungsten-bearing quartz veins in the ChongYu-You concentrated mineral area in Gannan region and its geological significance. *Acta Petrol. Sin.* **2008**, *82*, 932–940.
54. Liu, Y.; Hu, Z.; Gao, S.; Günther, D.; Xu, J.; Gao, C. In situ, analysis of major and trace elements of anhydrous minerals by LA-ICP-MS without applying an internal standard. *Chem. Geol.* **2008**, *257*, 34–43. [[CrossRef](#)]
55. Paton, C.; Hellstrom, J.; Paul, B.; Woodhead, J.; Hergt, J. Iolite: Freeware for the visualisation and processing of mass spectrometric data. *J. Anal. At. Spectrom.* **2011**, *26*, 2508–2518. [[CrossRef](#)]
56. Sardi, F.G.; Heimann, A. Pegmatitic beryl as indicator of melt evolution: Example from the Velasco district, Pampeana pegmatite province, Argentina, and review of worldwide occurrences. *Can. Mineral.* **2014**, *52*, 809–836. [[CrossRef](#)]
57. Giuliani, G.; Cheilletz, A.; Zimmermann, J.L.; Cheilletz, A.; Arboleda, C.; Charoy, B.; Goget, P.; Frontan, F.; Giars, D. Fluid composition, δD of channel H₂O, and $\delta^{18}O$ of lattice oxygen in beryls: Genetic implications for Brazilian, Colombian, and Afghanistani emerald deposits. *Int. Geol. Rev.* **1997**, *39*, 400–424. [[CrossRef](#)]
58. Zhao, T.X.; Chen, W.D.; Yin, T. EPMA quantitative analysis of beryllium mineral beryl. *Acta Miner. Sin.* **2019**, *39*, 169–175.
59. Turner, D.; Groat, L.A.; Hart, C.J.R.; Mortensen, J.K.; Linnen, R.L.; Giuliani, G.; Wengzynowski, W. Mineralogical and geochemical study of the True Blue aquamarine showing, southern Yukon. *Can. Mineral.* **2007**, *45*, 203–227. [[CrossRef](#)]
60. Hawthorne, F.C.; Černý, P. The alkali-metal positions in Cs–Li beryl. *Can. Mineral.* **1977**, *15*, 414–421.
61. Sherriff, B.L.; Grundy, H.D.; Hartman, J.S.; Hawthorne, F.C.; Černý, P. The incorporation of alkalis in beryl: Multi-nuclear MAS NMR and crystal-structure study. *Can. Mineral.* **1991**, *29*, 271–285.
62. Artioli, G.; Rinaldi, R.; Stahl, K.; Zanazzi, P.F. Structure refinements of beryl by single-crystal neutron and X-ray diffraction. *Am. Mineral.* **1993**, *78*, 762–768.
63. Černý, P. Mineralogy of beryllium in granitic pegmatites. *Mineral. Geochem.* **2002**, *50*, 405–444. [[CrossRef](#)]
64. Hawthorne, F.C.; Huminicki, D.M.C. The crystal chemistry of beryllium. *Rev. Mineral. Geochem.* **2002**, *50*, 333–403. [[CrossRef](#)]
65. Lum, J.E.; Viljoen, F.; Cairncross, B.; Frei, D. Mineralogical and geochemical characteristics of BERYL (AQUAMARINE) from the Erongo Volcanic Complex, Namibia. *J. Afr. Earth Sci.* **2016**, *124*, 104–125. [[CrossRef](#)]
66. Liu, Y.; Deng, J.; Sun, D.; Zhou, Y. Morphology and genesis typomorphism of minerals in W–Sn–Be deposit of Huya, Sichuan. *Geosci. J.* **2007**, *32*, 75–81.

67. Uher, P.; Chudík, P.; Bacik, P. Beryl composition and evolution trends: An example from granitic pegmatites of the beryl-columbite subtype, Western Carpathians, Slovakia. *J. Geosci.* **2010**, *55*, 69–80. [[CrossRef](#)]
68. Qin, K.Z.; Zhou, Q.F.; Tang, D.M.; Wang, R.C. Types, internal structure patterns, mineralization and prospects of rare-element pegmatites in East Qinling Mountain in comparison with feature of Chinese Altay. *Miner. Depos.* **2019**, *38*, 970–982.
69. Tang, Y.; Qin, S.X.; Zhao, J.Y.; Lü, Z.H.; Liu, X.Q.; Wang, H.; Chen, J.Z.; Zhang, H. Solubility of rare metals as a constraint on mineralization of granitic pegmatite. *Earth Sci. Front.* **2022**, *29*, 81–92.
70. Zhao, K.H. Mineralogy and Metallogenic Characteristics of Beryl in Pingjiang, Hunan Province, China. Master's Thesis, China University of Geosciences, Beijing, China, 2021.
71. Xu, X.W.; Hong, T.; Li, H.; Ke, Q.; Chen, J.Z.; Liu, S.K.; Zhai, M.G. Concept of high-temperature granite-pegmatite Li-Be metallogenic system with a primary study in the middle Altyn-Tagh. *Acta Petrol. Sin.* **2020**, *36*, 3572–3592.
72. Dai, Z.W. Study on Mineralization of the Cuonadong Be-Sn-W Polymetallic Deposit, Tibet, China. Ph.D. Thesis, Chengdu University of Technology, Chengdu, China, 2020.
73. Dai, Z.W.; Li, G.M.; Ding, J.; Zhang, L.K.; Cao, H.W.; Zhang, Z.; Liang, W. Chemical and Boron Isotopic Composition, and Significance of Tourmaline from the Cuonadong Tourmaline Granite, Tibet. *Earth Sci.* **2019**, *44*, 1849–1859.
74. Wood, S.A. Theoretical prediction of speciation and solubility of beryllium in hydrothermal solution to 300 °C at saturated vapor-pressure—Application to Bertrandite Phenakite Deposits. *Ore Geol. Rev.* **1992**, *7*, 249–278. [[CrossRef](#)]
75. Long, Z.Y.; Yu, X.Y.; Zheng, Y.Y. Ore formation of the Dayakou emerald deposit (Southwest China) constrained by chemical and boron isotopic composition of tourmaline. *Ore Geol. Rev.* **2021**, *135*, 104208. [[CrossRef](#)]
76. Rao, C.; Wang, R.C.; Hu, H. Paragenetic assemblage of beryllium silicates and phosphates from the Nanping granite pegmatite dyke; Fujian province southeastern China. *Can. Mineral.* **2011**, *49*, 1175–1187. [[CrossRef](#)]
77. Ge, Z.B. Emerald orebody in metagranite-greisen beryl deposit. *Geol. Explor.* **1983**, *6*, 24–31.
78. Rao, C.; Wang, R.C.; Hu, H. Electron-Microprobe Compositions and Genesis of Beryls from the Nanping No. 31 Granitic Pegmatite (Fujian Province, Southeastern China). *Geol. J. China Univ.* **2009**, *15*, 496–505.
79. Wu, F.Y.; Liu, Z.C.; Liu, X.C. Himalayan leucogranite: Petrogenesis and implications to orogenesis and plateau uplift. *Acta Petrol. Sin.* **2015**, *31*, 1–36.